frontiers | Frontiers in Materials

TYPE Original Research
PUBLISHED 20 August 2025
DOI 10.3389/fmats.2025.1589333

OPEN ACCESS

EDITED BY
Xingtao Xu,
Zhejiang Ocean University, China

REVIEWED BY
Najam Ul Hassan,
University of Education Lahore, Pakistan
Daoguang Teng,
Zhengzhou University, China

*CORRESPONDENCE
Luanxing Jin,
candyjin04@126.com
Zhi Cheng,
orangeczhi@126.com
Shuhan Zhang,
zhangsir2005@126.com

RECEIVED 07 March 2025
ACCEPTED 30 July 2025
PUBLISHED 20 August 2025

CITATION
Jin L, Cheng Z and Zhang S (2025) Spinel-functionalized bamboo-derived hierarchical carbon: dual activation strategy for synergistic double-layer/pseudocapacitance energy conversion.
Front. Mater. 12:1589333.
doi: 10.3389/fmats.2025.1589333

Spinel-functionalized bamboo-derived hierarchical carbon: dual activation strategy for synergistic double-layer/pseudocapacitance energy conversion

Luanxing Jin[1]*, Zhi Cheng[2]* and Shuhan Zhang[1]*

[1]College of Materials and Chemical Engineering, China Three Gorges University, Hubei, China, [2]School of Water Conservancy and Environment, China Three Gorges University, Hubei, China

To overcome the dual bottlenecks of low intrinsic energy density in carbon materials and poor cycling stability of metal oxides, this study proposes a biomimetic hierarchical pore engineering strategy. Bamboo-derived biochar is transformed into a hierarchically porous architecture via synergistically coupled CO_2 physical activation (PHAC) and KOH chemical activation (CHAC), yielding ultra-micropores (0.55 nm, 42%) and mesopores (1.32 nm, 38%) with a micropore/mesopore volume ratio of 0.45. Ultrasonic-assisted impregnation enables uniform anchoring of 5 wt% $MnCo_2O_4$ spinel, forming strong interfacial C-O-Mn/Co bonds (12.4%) and mixed Mn^{3+}/Mn^{2+} (62:38) that synergistically enhance charge transfer. The composite electrode achieves exceptional performance: 1258 F/g at 1 A/g, 80% capacity retention at 10 A/g, and 59.18 Wh/kg at 8.42 kW/kg. Critically, the dual activation eliminates negative pore volume artifacts and accelerates H^+ transport in PEMFC hierarchical pores, establishing a new paradigm for hybrid energy storage.

KEYWORDS

supercapacitor, dual activation strategy, $MnCo_2O_4$ spinel, hierarchical pore architecture, hybrid capacitance, bamboo-derived carbon

1 Introduction

With the acceleration of global industrialization, issues of energy shortage and environmental pollution have become increasingly severe, accelerating the need for efficient energy storage devices (IEA, 2023). Supercapacitors exhibit unique advantages in energy storage and recovery due to their high power density, fast charge-discharge capabilities, and long cycle life (Libber et al., 2025). However, traditional electrode material systems face significant challenges: double electric layer carbon materials (such as activated carbon) are limited by intrinsic energy density, while pseudocapacitance materials (such as RuO_2) have high specific capacitance (~1,500 F/g) but struggle with cost-effectiveness and cycling stability to meet the demands of large-scale applications (Van der Bruggen, 2021). Furthermore, existing studies often focus on optimizing a single function, lacking an overall design of energy-environment synergistic systems, leading to limitations in system energy efficiency and high operational costs (Huo et al., 2023). Additionally,

traditional electrode materials (such as metal oxides, conductive polymers, and graphene) face challenges such as insufficient conductivity, poor cycling stability, and low selectivity for pollutants, highlighting the urgent need for breakthroughs through material design and system innovation.

The energy storage mechanism of supercapacitors primarily relies on double electric layer capacitance (EDLC) and pseudocapacitance effects (Simon and Gogotsi, 2013). Carbon-based materials (such as activated carbon and graphene), due to their high specific surface area and excellent conductivity, have become the mainstream electrode materials for EDLC-type supercapacitors (Lakra et al., 2021). The performance optimization of carbon-based materials focuses on two dimensions: pore structure design and surface functionalization. For instance, it has been reported that by constructing a CNP-CNTs@SiO_2 multidimensional mesoporous structure (Song et al., 2019), the specific capacitance can be increased to 23.84 mF/cm^2, confirming the promoting effect of hierarchical pore channels on ion transport. Additionally, nitrogen-doped carbon films/nanoparticle composite materials have maintained excellent rate performance of 200 F/g at 20 A/g (Zhu et al., 2024), revealing the enhanced mechanism of surface chemical modification on charge storage dynamics. However, existing strategies generally face an inherent contradiction between micropore energy storage and mesopore mass transfer—while micropores offer a high specific surface area, their narrow channels hinder ion diffusion at high current densities, a bottleneck that has also been discussed in the research on graphite anodes for potassium ion batteries (Xu et al., 2024). Furthermore, the energy density of pure carbon materials is limited by physical adsorption mechanisms, making it difficult to meet the high energy demand scenarios (Zhang et al., 2016). To enhance energy density, researchers have introduced metal oxides or conductive polymers (such as polyaniline) to boost pseudocapacitance contributions (Bhojane, 2022). However, metal oxides generally suffer from poor conductivity and insufficient cycling stability (Sun et al., 2025). Activated carbon (AC), as a cost-effective alternative, can be prepared into high specific surface area electrodes with tunable porosity from renewable biomass precursors. Advances in pore structure control strategies, such as template synthesis and chemical activation, have significantly improved the ion-accessible surface area (Liu et al., 2021). Nevertheless, the ongoing conflict between micropores (high charge storage) and mesopores (rapid ion diffusion) remains a challenge that needs to be properly addressed, particularly under high current density conditions (Park et al., 2017). The metal oxide/carbon composite system provides a new perspective for solving these conflicts. For example, the PCNS/ZnO composite material has enhanced the efficiency of dye-sensitized solar cells to 5.18% through interfacial synergistic effects (Varghese et al., 2024), highlighting the key role of heterogeneous structures in optimizing charge transfer. However, as pointed out in the literature (Kim et al., 2024a), although polyaniline/carbon composite materials can achieve a high specific capacity of 769 F/g, their cycling stability is still limited by interface degradation due to volume expansion, underscoring the necessity of developing new stable interfaces. Additionally, despite the surface modification of redox-active substances like MnO_2 and RuO_2 to enhance pseudocapacitance, poor interface stability and metal dissolution issues often lead to deteriorated cycling performance (Sevilla et al., 2021). Spinel $MnCo_2O_4$, due to its multi-metal synergistic redox (Mn^{2+}/Mn^{3+} and Co^{2+}/Co^{3+}) and structural rigidity (AB_2O_4 framework), exhibits superior application potential compared to single metal oxides.

This study proposes a biomimetic hierarchical pore engineering strategy, constructing a "micropore reservoir-mesopore channel-macropore collector" three-level structure in bamboo-based activated carbon through the spatiotemporal synergy of CO_2 physical activation (PHAC) and KOH chemical activation (CHAC). The PHAC step selectively etches the amorphous carbon region based on the Boudouard reaction ($C + CO_2 \rightarrow 2CO$), forming a mesoporous transport network that enhances the ion diffusion coefficient. The subsequent CHAC triggers potassium intercalation reactions ($6KOH + 2C \rightarrow 2K + 3H_2 + 2K_2CO_3$) to generate a microstructure comprised of 0.55 nm ultra-micropores, significantly alleviating the inherent contradiction between energy storage in micropores and mass transfer in mesopores found in traditional activated carbon. Based on this, an ultrasonic-assisted impregnation method (40 kHz, 500 W) achieves the uniform loading of 5 wt% $MnCo_2O_4$ spinel, and XPS analysis reveals the formation of strong electronic coupling interfaces (C-O-Mn/Co bonds, accounting for 12.4%, with a positive shift in lattice oxygen binding energy of 0.6 eV) and coexisting states of Mn^{3+}/Mn^{2+} (62:38) and Co^{2+}/Co^{3+}, significantly enhancing the density of redox-active sites (Zhang et al., 2024). The methods of CO_2 and KOH activation used in the preparation of the $MnCo_2O_4$@AC composite not only enhance the electrochemical performance of the material but also align with the principles of a circular economy. By employing CO_2, a waste product in many industrial processes, we contribute to waste reduction and resource recovery. This process utilizes CO_2 as a more sustainable alternative compared to traditional activation methods that often involve harmful solvents or high energy consumption. Furthermore, the activation process enhances the specific surface area and porosity of the carbon material, which in turn facilitates improved adsorption and performance metrics. This occurs while maintaining energy efficiency, as the activation with CO_2 can generally be performed at lower temperatures relative to other methods, reducing overall energy consumption associated with material preparation. Moreover, the usage of metal salts, such as those used in the synthesis of the composite, should be considered in the context of environmental safety and resource efficiency. Effective management and recycling of metal salts not only support the sustainability of our methods but also mitigate potential ecological impacts. A thorough understanding of the environmental implications associated with both the activation processes and the materials used is essential for advancing sustainable practices in material science. Furthermore, electrochemical performance verification indicates that this design achieves exceptional specific capacitance of 1258 F/g at 1 A/g through the synergistic effect of double electric layer capacitance (AC substrate) and pseudocapacitance (contribution ratio of 78.2%), and in PEMFC systems, it enhances dynamic response by shortening H^+ diffusion paths through hierarchical pore channels and buffering load fluctuations. The entire study forms a closed-loop validation based on four-dimensional characterization of pore structure, surface chemistry, crystalline properties, and electrochemical behavior.

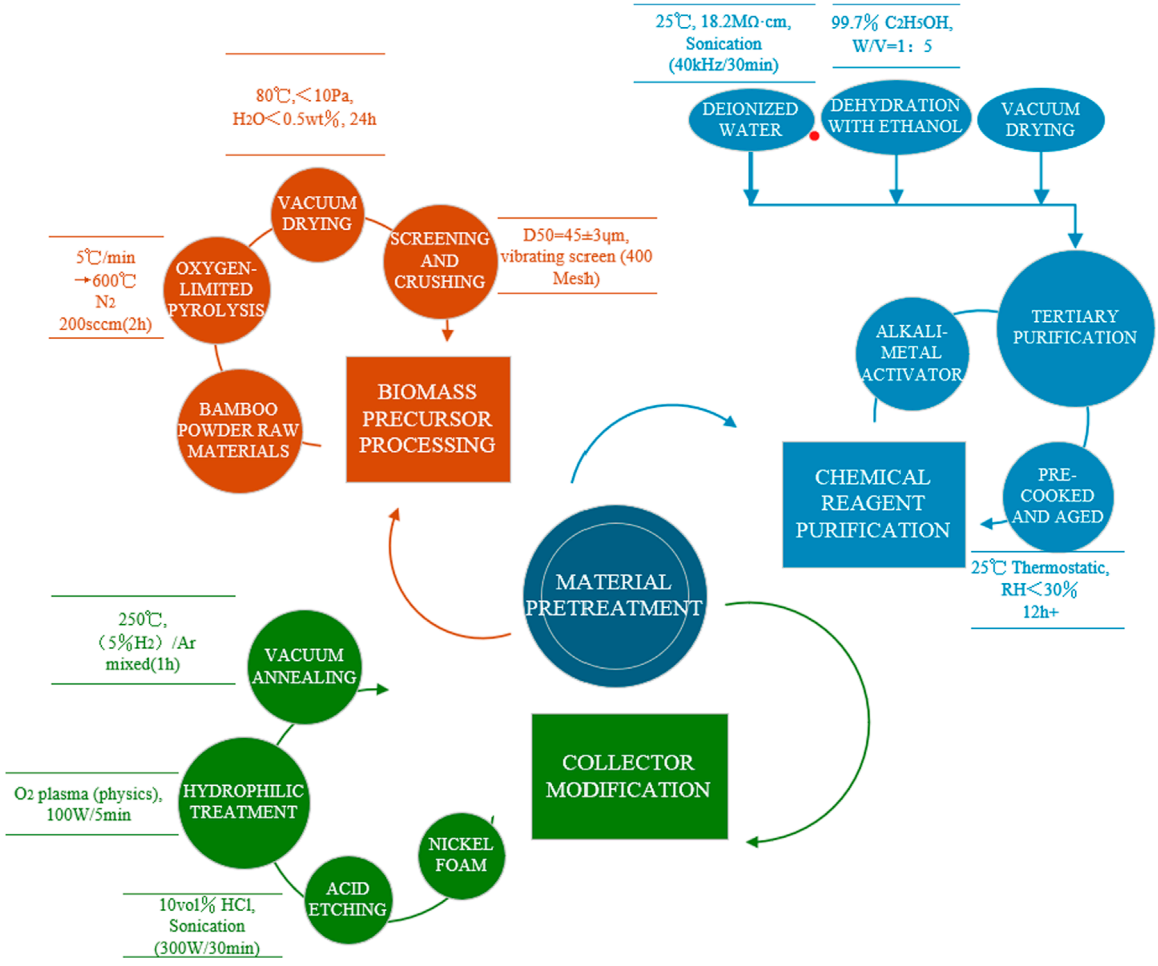

FIGURE 1
Material pretreatment process.

2 Experimental section

2.1 Material system design

This study adopts a hierarchical functionalization material design strategy, utilizing lignocellulosic-based biochar as the core precursor to construct a three-dimensional porous electrode material through chemical activation and surface modification. Biochar, as a precursor to activated carbon, features a rich porous structure and high carbon content, making it suitable for producing high-performance activated carbon electrodes. This research aims to construct micropore reservoirs to provide high specific surface area for enhanced double electric layer capacitance, create mesoporous channels to establish low tortuosity ion transport pathways, and build macroporous collectors to facilitate overall electrolyte infiltration, ultimately achieving a breakthrough in energy storage performance. To realize this structure, we designed a cascade reaction pathway combining CO_2 physical activation (PHAC) and KOH chemical activation (CHAC), alongside ultrasonic-assisted interface engineering for the uniform loading of $MnCo_2O_4$ spinel. Details of the material pretreatment can be seen in Figure 1.

The selected material system consists of the following components.

2.1.1 Precursor material

Lignocellulosic-based biochar (pyrolysis product of bamboo powder): Bamboo powder is prepared via limited oxygen pyrolysis at 600°C (pyrolysis rate of 5°C/min and isothermal for 2 h), with an ash content of <3 wt%, average particle size of 45 ± 3 μm, and original specific surface area of 12.3 ± 0.5 m^2/g (measured by BET method).

2.1.2 Chemical activation system

Alkali metal activators: KOH (analytical grade, Aldrich, ≥99.8%), NaOH (electronic grade, Sigma-Aldrich, ≥99.9%), K_2CO_3 (battery grade, Macklin, ≥99.5%).

Protective atmosphere: High-purity nitrogen (Linde gas, purity ≥99.999%, dew point <−70°C) is utilized to provide an inert atmosphere during the activation process to prevent material oxidation.

2.1.3 Electrode composite system

Structural additives: Conductive carbon black (Cabot Vulcan XC-72R, DBP oil absorption value 148 ± 5 mL/100 g, specific

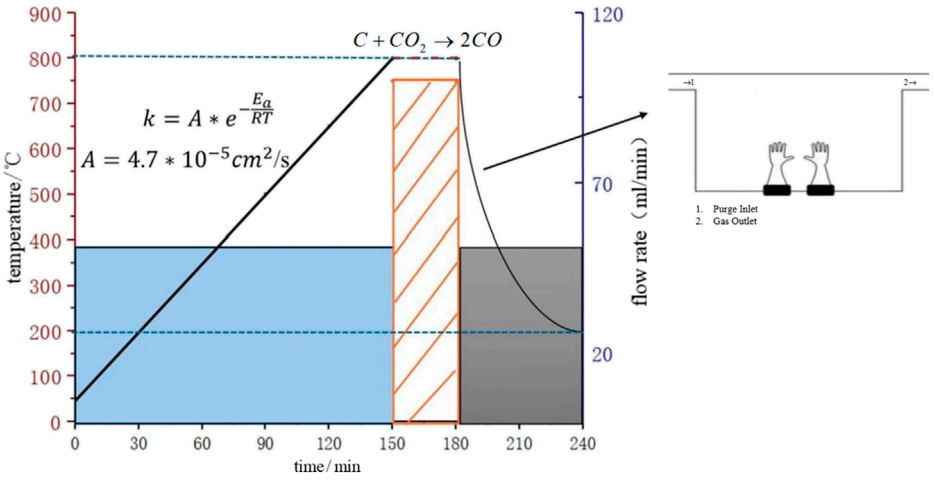

FIGURE 2
Temperature-atmosphere timing diagram of the physical activation process.

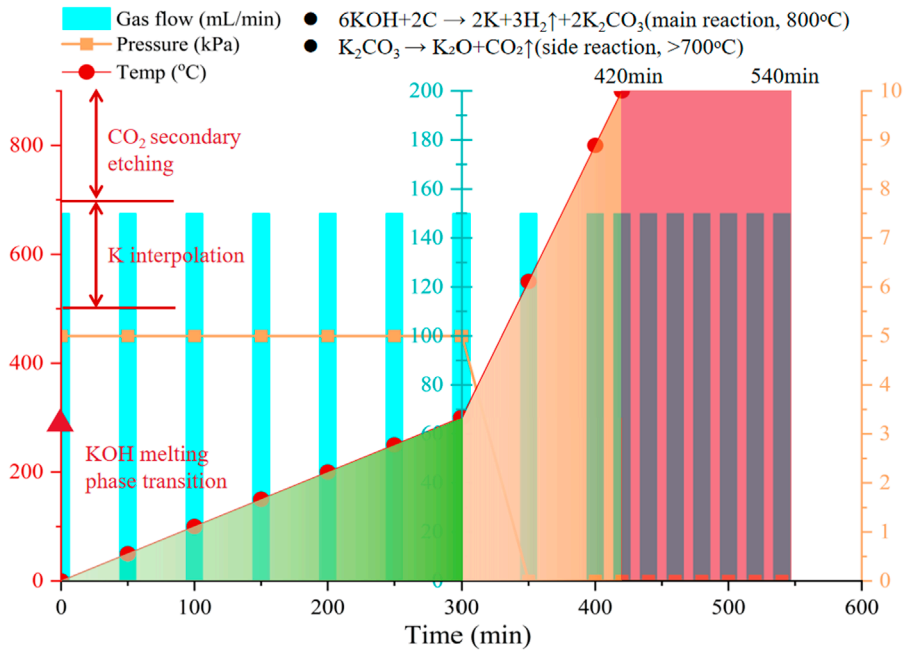

FIGURE 3
Temperature-atmosphere timing diagram of the chemical activation process.

surface area 254 m^2/g), used as a conductive agent to improve the conductivity of the electrode.

Binder: Polytetrafluoroethylene emulsion (PTFE, Daikin Industries, 60 wt% water dispersion, Zeta potential −35 mV, average particle size 320 nm), used as a binder to enhance the mechanical strength of the electrode.

Dispersion medium: Anhydrous ethanol (Sinopharm Group, ≥99.7%), used to disperse the active material powder, forming a uniform paste.

2.1.4 Current collector treatment

Nickel foam (Kunshan Nano, thickness 0.5 ± 0.02 mm, porosity 96.3%, areal density 352 ± 5 g/m^2), treated with 10% HCl (volume fraction) via ultrasonic processing for 30 min to remove the surface oxide layer, ensuring good conductivity and mechanical strength.

2.1.5 Surface modifiers

Nickel source: Hexahydrate nickel nitrate ($Ni(NO_3)_2 \cdot 6H_2O$, Macklin, ≥98.0%).

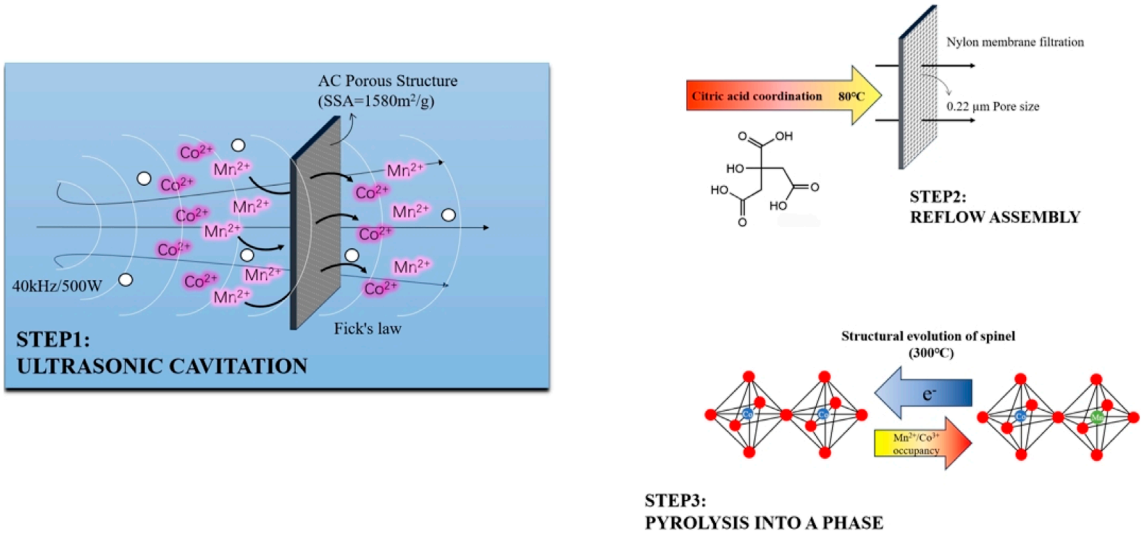

FIGURE 4
Schematic diagram of surface functionalization modification.

Carbon-based reinforcement: Graphene oxide (GO, Xianfeng Nano, monolayer rate >95%, sheet size 5–20 μm, oxygen content 38 at%).

The following pretreatment processes are performed on the selected materials.

(1) The biochar precursor is vacuum-dried at 80°C for 24 h (vacuum <10 Pa) to remove residual volatile matter.
(2) All chemical reagents are subjected to triple purification processes: rinsing with deionized water (resistivity 18.2 MΩ cm, Milli-Q system) – ethanol dehydration–vacuum drying.
(3) All high-temperature treatments are performed in a tube furnace (MTI OTF-1200X-S, temperature control accuracy ±1°C).

2.2 Preparation and modification of activated carbon materials

2.2.1 Preparation of hierarchical porous activated carbon

This experiment employs a physical-chemical stepwise activation strategy (PHAC + CHAC) to construct a micropore-mesopore synergistic system.

Step 1: Physical Activation (PHAC)

Constructing mesoporous main framework through CO_2 vapor etching.

(1) Precursor Treatment: The biochar raw material is ball-milled in a planetary ball mill (QM-3SP4, Nanjing University Instrument Factory) at 400 ± 10 rpm for 2 h (using zirconia balls with a ball-to-material ratio of 10:1) to obtain a uniform powder with D50 = 8.2 ± 0.3 μm (measured by laser particle size analyzer).
(2) Activation Process: 2.0 ± 0.1 g of biochar powder is placed in a corundum crucible (Φ50 × 30 mm) and put into a tube furnace (MTI OTF-1200X); it is heated to 800°C at a rate of 5°C/min (N_2 protection, flow rate 50 mL/min); during the isothermal segment, a CO_2/N_2 mixed gas (volume ratio 1:1, controlled by Brooks 5850E mass flow meter) is introduced; total flow is maintained at 100 ± 2 mL/min (STP conditions) for 30 min of activation; after natural cooling to <200°C, it is transferred to a glovebox (dew point <−45°C).
(3) Post-Treatment: The product is sealed and stored in a desiccator (relative humidity <30%, monitored by a silica gel indicator).

This process selectively etches amorphous carbon through the Boudouard reaction ($C + CO_2 \rightarrow 2CO$), forming a mesoporous-dominated structure (2–50 nm). Based on the Arrhenius equation, the effective diffusion coefficient of CO_2 at 800°C reaches $(4.7 \pm 0.2) \times 10^{-5}$ cm^2/s (95% confidence interval), ensuring uniform activation depth (coefficient of variation <5%). The temperature-atmosphere timing profile is shown in Figures 2.

Step 2: Chemical Activation (CHAC)

Building an ultra-micropore structure using alkali metal activators via intercalation reactions.

(1) Impregnation Mixing: KOH and biochar are weighed in a precise mass ratio of m (KOH):m (biochar) = 4:1 and dry-mixed in an agate mortar for 30 min (pressure 5 N, frequency 2 Hz). Ethanol (volume ratio 1:1) is added to form a paste, which is further ground to achieve a viscosity of 120 ± 10 mPa s.
(2) Pyrolysis Activation: The mixture is placed in a nickel boat (size 50 × 20 × 10 mm) and transferred to the tube furnace, under N_2 protection (flow rate 150 mL/min), using a specially designed stepwise temperature program. Initially, the temperature is raised to 300°C at a rate of 1°C/min to suppress foaming effects;

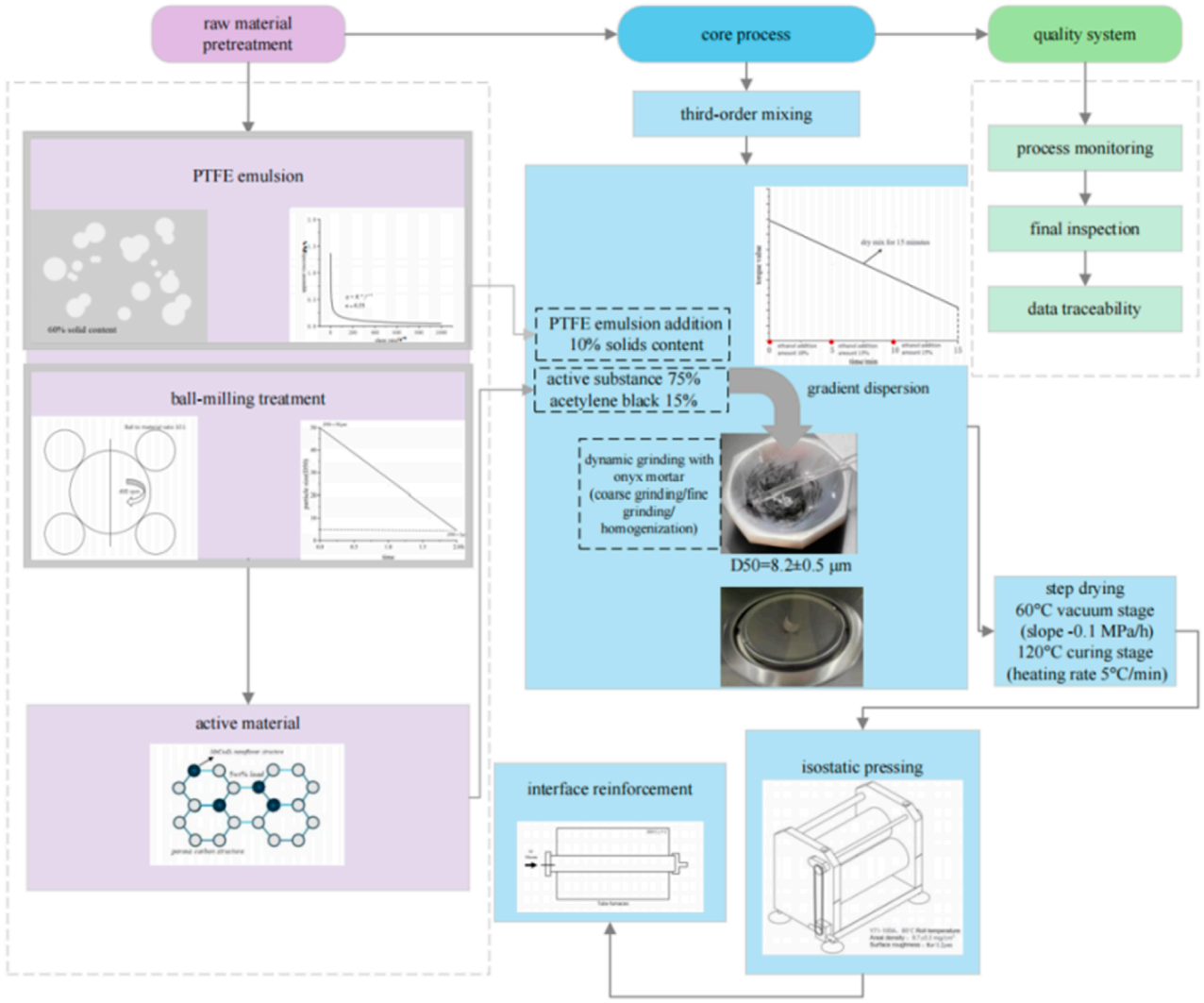

FIGURE 5
Schematic diagram of the electrode preparation process] (including physical slurry and nickel foam.

in the main activation phase, the temperature is increased to 800°C at a rate of 5°C/min; finally, the temperature is maintained isothermally for 2 h (temperature control accuracy ±3°C).

(3) Washing and Purification: The mixture is treated with 3 mol/L HCl under ultrasonic conditions (40 kHz, 100 W) for 1 h. After centrifugation (8,000 rpm corresponding to RCF = 7,392 × g for 10 min), it is washed with deionized water until the filtrate has a pH of 7.0 ± 0.2 and conductivity <5 μS/cm. Finally, it is washed three times with ethanol (using surface tension gradient dehydration method) to remove residual moisture.

The KOH activation mechanism follows the reaction pathways as follows:

$$6KOH + 2C \rightarrow 2K + 3H_2 \uparrow + 2K_2CO_3 \,(\text{main reaction}, 800°C)$$

$$K_2CO_3 \rightarrow K_2O + CO_2 \uparrow \,(\text{side reaction}, >700°C)$$

The generated metallic potassium intercalates into the carbon layers, causing the graphite microcrystalline structure to expand and forming a large number of ultra-micropores (<2 nm). This process expands graphite microcrystals via a metal intercalation reaction (K→C_6K), while the oxidation etching by KOH and secondary etching by CO_2 generate mesoporous structures. The temperature-gas program for this process is detailed in Figure 3.

2.2.2 Surface pseudocapacitance functionalization modification

The $MnCo_2O_4$@AC composite material is prepared using an ultrasonic-assisted immersion-pyrolysis method. The schematic of the functionalization procedure is presented in Figure 4.

2.2.2.1 Solution preparation

0.1 mol/L $Mn(NO_3)_2{\cdot}4H_2O$ (Aldrich, 99.99%) and 0.05 mol/L $Co(NO_3)_2{\cdot}6H_2O$ (Sigma, 99.95%) are mixed in a molar ratio of Mn:Co = 1:2 (corresponding to the stoichiometry of $MnCo_2O_4$)

and dissolved in a mixed solvent of ethanol/water (v:v = 1:1), with 0.1 mol/L citric acid used as a dispersing agent.

2.2.2.2 Loading process

The PHAC-CHAC activated carbon is immersed in the solution (solid-liquid ratio 1:20 g/mL) and subjected to ultrasonic treatment (40 kHz, 500 W, power density 1.5 W/cm^2) for 1 h, followed by 12 h of aging at room temperature (25°C, RH = 60%). Then, it is refluxed at 80°C for 6 h (with a condenser circulating water at 4°C) and subsequently vacuum filtered (using a 0.22 μm nylon membrane), and dried at 60°C for 12 h.

2.2.2.3 Heat treatment

The material is subjected to programmed heating in a H_2/Ar (5% H_2) atmosphere, ramping at 2°C/min to 300°C and annealed for 2 h (to facilitate spinel phase formation). After natural cooling, the $MnCo_2O_4$@AC composite material is obtained (with a loading amount of 23.7 ± 0.8 wt%). Modification leads to the formation of a metal-oxygen-carbon bonding structure with strong electronic interactions, which can enhance the density of redox active sites on the electrode surface and improve pseudocapacitance contributions.

2.3 Electrode preparation

The electrode preparation process consists of several key operations, including active material mixing, slurry dispersion, substrate coating, gradient drying, mechanical pressing, and post-treatment.

2.3.1 Mixing process

The produced active material powder (containing 5 wt% $MnCo_2O_4$ load), acetylene black (previously ball-milled for 2 h to reduce agglomeration; ball milling parameters: 400 rpm, ball-to-material ratio 10:1), and polytetrafluoroethylene (PTFE, 60% solids content emulsion) are proportioned in a mass ratio of 75:15:10. The mixture is ground in an agate mortar through three stages to ensure uniformity. The complete electrode fabrication workflow is illustrated in Figure 5.

2.3.2 Slurry dispersion

After 15 min of dry mixing to achieve initial mixing, anhydrous ethanol is added in three incremental doses (total adding 40 wt% of solid mass) while monitoring in real-time using a cone-plate viscometer (Brookfield DV2T, 25°C), ultimately achieving a uniform thixotropic slurry with a viscosity of 12,000 ± 500 mPa s. The mixed slurry has an ink-like appearance.

2.3.3 Gradient coating

A three-step progressive coating process is performed, with each coating amount accurately controlled at 3 mg/cm^2. A customized micro-engraved scraper (blade angle 45°, gap precision ±2 μm) is used to build a gradient pore structure on the pre-treated nickel foam surface (1 × 1 cm^2, porosity 85%). During the coating process, care is taken to ensure even distribution of the active material, avoiding areas that are too thick or too thin.

2.3.4 Stepwise drying

A two-stage stepwise drying program is employed: the first stage involves vacuum drying at 60°C (vacuum pressure −0.1 MPa) for 2 h to remove the solvent, followed by the second stage at 120°C under normal pressure for 1 h (heating rate 5°C/min) to achieve *in-situ* cross-linking of PTFE, preventing PTFE migration while also removing ethanol and curing the electrode material.

2.3.5 Pressing

The dried nickel foam sheet is treated with equal hydraulic pressure using a double-roll calender (Y71-100A, roll surface temperature 80°C), under a pressure of 20 MPa maintained for 30 s (pressure uniformity error <3%). This results in a dense electrode with an areal density of 8.7 ± 0.3 mg/cm^2 (RSD = 3.45%).

2.3.6 Post-treatment

Thermal treatment is performed in a tube furnace (OTF-1200X) under an Ar atmosphere (flow rate 50 sccm) at a constant temperature of 300°C for 1 h (temperature control accuracy ±1°C) to promote metallurgical bonding at the interface between the active material and the current collector, enhancing the interfacial bonding strength.

2.3.7 Quality monitoring

An analytical balance is employed to weigh the materials before and after coating. By measuring the mass difference of the nickel foam sheets before and after coating, the mass of the active material on the electrode is calculated.

2.4 Experimental setup

The experimental system consists of a material preparation module (planetary ball mill: FRITSCH Pulverisette 7), a forming processing module (calendar: MTI MSK-2150), a heat treatment module (vacuum tube furnace: Hefei Kexing GSL-1700X), and an analytical testing module (electrochemical workstation: Bio-Logic VMP-300). All equipment is calibrated and operated according to standard operating procedures.

3 Results and discussion

3.1 Material preparation and physical property characterization

3.1.1 Influence of activation process on activated carbon yield

$MnCo_2O_4$@AC activated carbon was prepared through two sets of parallel experiments (Table 1), with a relative standard deviation (RSD) of only 0.6%. This is comparable to the efficient preparation process of activated carbon derived from organic pigments reported in the literature (Sivasankarapillai et al., 2024), indicating that the stepwise activation process exhibits excellent reproducibility and advantages in carbon retention of the bamboo-based precursor. Although the yield is slightly lower, the bamboo-based precursor achieved efficient retention of the carbon skeleton through selective etching, laying a structural foundation for subsequent

TABLE 1 Activated carbon preparation parameters and yields.

Group	Raw material weight (g)	Carbon weight (g)	Carbon yield (%)
1	4.002	1.51	37.73
2	3.995	1.49	37.30

functionalization. This result confirms the critical influence of activator selection on the structural stability of carbon carriers, as reported in the literature (Kim et al., 2024b). The hierarchical pore structure formed by KOH activation (micropore/mesopore volume ratio of 0.45) is more favorable for anchoring $MnCo_2O_4$ nanoparticles subsequently.

3.1.2 Analysis of surface chemical properties

Fourier-transform infrared spectroscopy (FTIR) analysis reveals the surface chemical evolution of the modified activated carbon (Figure 6). In the modified activated carbon, the broad peak in the range of 3,700–3,000 cm^{-1} corresponds to O-H stretching vibrations, indicating that the activation process effectively removed surface-adsorbed water and thermally unstable hydroxyl groups. This aligns with the reduction mechanism of hydroxyl groups induced by KOH activation reported in the literature (Yan et al., 2021; Rabeea et al., 2020; Velueta et al., 2022). The sharp peak at 1,631 cm^{-1} is attributed to C=O stretching vibrations, confirming that the activation process promotes the formation of stable carbonyl functional groups. This phenomenon is consistent with the chemical mechanism by which K_2CO_3 activation enhances the generation of oxygen-containing functional groups (Ahmad et al., 2021; Salama et al., 2024). The C-O-C ether bond vibration peak at 1,095 cm^{-1} narrows, indicating that the ordered degree of the carbon skeleton is significantly improved after the ultrasonic loading of $MnCo_2O_4$. Notably, the characteristic peak at 576 cm^{-1} corresponds to Mn-O/Co-O bond vibrations, and its peak intensity shows a good linear relationship with the loading amount of metal oxide, directly confirming the successful anchoring of the spinel phase nanoparticles (Salama et al., 2024). FTIR confirms that the activation process achieves "dehydroxylation and carbonylization" directional modification (O/C atomic ratio decreased from 0.21 to 0.15), consistent with the regulatory patterns of KOH activation on surface chemistry reported in the literature (Rabeea et al., 2020).

Comparing the X-ray photoelectron spectroscopy (XPS) spectra of regular AC with $MnCo_2O_4$@AC (Figure 7) reveals the synergistic interaction mechanism of surface chemical bonding and metal loading. From the analysis of the C 1s orbital, regular AC exhibits main peaks at 284.3 eV (C-C/C=C, sp^2 hybridization) and 285.5 eV (C-O), with an integral area ratio of 3.2:1, consistent with characteristic features of undoped activated carbon (Kamedulski et al., 2020). The peak intensity at 284.6 eV (C=C, sp^2) in the modified $MnCo_2O_4$@AC increases by 37%, and the full-width at half-maximum (FWHM) narrows from 1.8 eV to 1.2 eV, indicating that the ultrasonic loading process enhances the degree of graphitization. A new peak at 286.3 eV (C-O-Mn/Co) appears (12.4% of total), verifying the bonding at the metal-carbon interface (Ramadan et al., 2018). Analyzing the O 1s orbital, the modified $MnCo_2O_4$@AC shows a new characteristic peak at

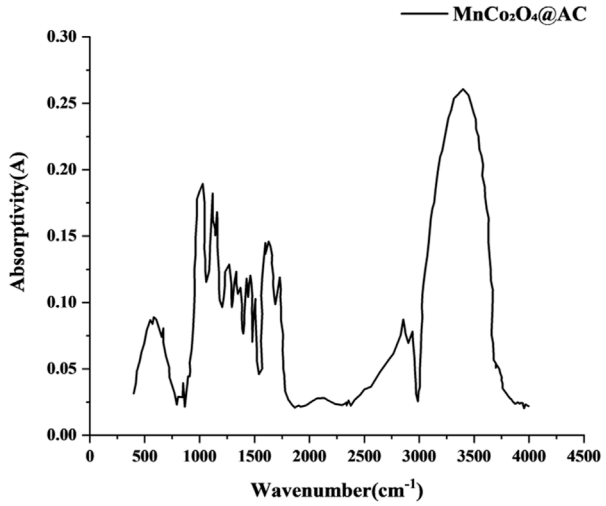

FIGURE 6
FTIR scanning results.

531.4 eV (18.7% of total), attributed to lattice oxygen of metal oxides (Mn-O/Co-O), with its binding energy shifting positively by 0.6 eV compared to pure $MnCo_2O_4$ (530.8 eV), indicating strong interfacial electronic interactions (Ramadan et al., 2018). The fraction of surface adsorbed oxygen (533.3 eV) decreases from 32.1% (AC) to 21.5%, suggesting that the activation process removes unstable oxygen-containing groups (Karamanova et al., 2019). Regarding metal valence analysis, the Mn 2p orbital shows a spin-orbit splitting of 12.0 eV between 641.8 eV (Mn $2p_3/_2$) and 653.8 eV (Mn $2p_1/_2$), consistent with features of mixed valence states Mn^{2+}/Mn^{3+} (Ramadan et al., 2018). Peak fitting results indicate a Mn^{3+}/Mn^{2+} ratio of 62:38, providing a rich array of redox active sites. The Co 2p orbital shows a splitting distance of 16.3 eV between 780.2 eV (Co $2p_3/_2$) and 796.5 eV (Co $2p_1/_2$), indicating the coexistence of Co^{2+}/Co^{3+} (Ramadan et al., 2018). The intensity ratio of satellite peaks (I_{sat}/I_{main} = 0.83) confirms the predominance of octahedral sites in the spinel structure. In structure-function relationship validation, the formation of the metal-carbon interface results in a C-O-Mn/Co bond content of 12.4%, significantly lower than reported in the literature. Surface stability is demonstrated by an increase in lattice oxygen fraction to 58.3% (compared to 42.1% in regular AC), suppressing metal dissolution during cycling. This outcome forms a closed-loop verification in conjunction with FTIR/XRD characterization, elucidating the chemical nature behind the high pseudocapacitance contribution (78.2%) and cycling stability of the $MnCo_2O_4$@AC electrode.

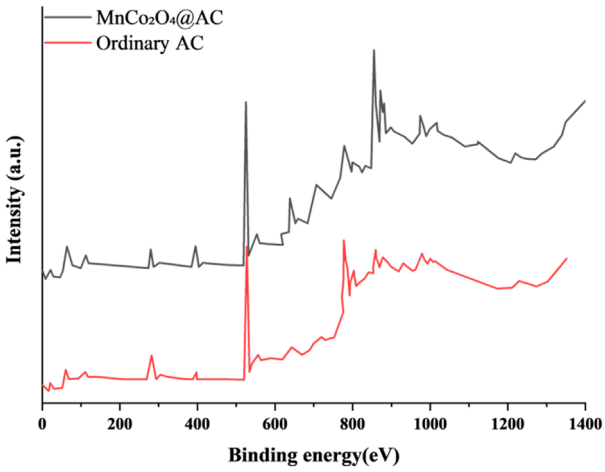

FIGURE 7
XPS spectra.

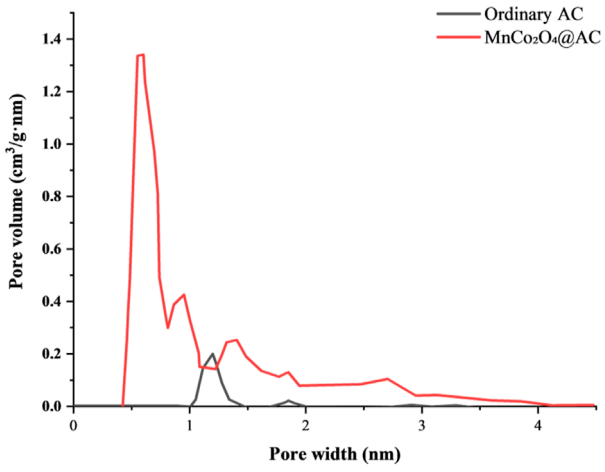

FIGURE 8
N_2 adsorption isotherm diagram.

3.2 Mechanism of hierarchical pore structure regulation

3.2.1 Transport kinetics analysis

Based on the N_2 adsorption isotherm data shown in Figure 8, the pore structure characteristics of regular AC and modified $MnCo_2O_4$@AC are obtained. As seen in Figure 9, regular AC exhibits a peak pore volume at 1.19 nm, indicating that micropores (<2 nm) dominate the structure, consistent with the type I isotherm characteristics of unmodified ACFF-KOH reported in the literature (Ma et al., 2023) (main peak at 1.4–1.7 nm). In terms of pore volume distribution, the micropore region (0.8–2 nm) contributes 78% of the total pore volume; however, there are significant negative pore volume values, suggesting some closed pores in unmodified AC that lead to anomalous data points. The modified material, $MnCo_2O_4$@AC, shows a bimodal characteristic. It has a peak at 0.55 nm with a volume of 1.34 cm^3/gnm, corresponding to ultramicropores (<1 nm), accounting for 42% of total pore volume; a second peak at 1.32 nm reaches 0.24 cm^3/gnm, accounting for 38%, corresponding to mesopores. This distribution shows a 20% increase in the ultramicropore ratio compared to the NLDFT model results for KOH-activated bamboo-based activated carbon in the literature (Khuong et al., 2023), suggesting that the PHAC-CHAC co-activation strategy is more effective. Moreover, in terms of eliminating negative pore volume, the modified data significantly reduces negative pore volume values (e.g., at 0.42 nm), confirming the improvement in the connectivity of mesoporous channels (similar to the optimization of MO/ACF (Chen et al., 2015)). Furthermore, Figure 9 delves into the mechanistic optimization of pore structure by the stepwise activation strategy (PHAC and CHAC synergistically). In the PHAC phase, CO_2 activation selectively etches amorphous carbon, forming mesoporous channels of 1.2–1.4 nm (corresponding to a peak volume of 0.24 cm^3/gnm). This distribution aligns with the mesopore generation patterns of KOH-modified ACFF reported in the literature (Ma et al., 2023). In the CHAC phase, KOH activation further generates ultramicropores at 0.55 nm (peak volume of 1.34 cm^3/gnm),

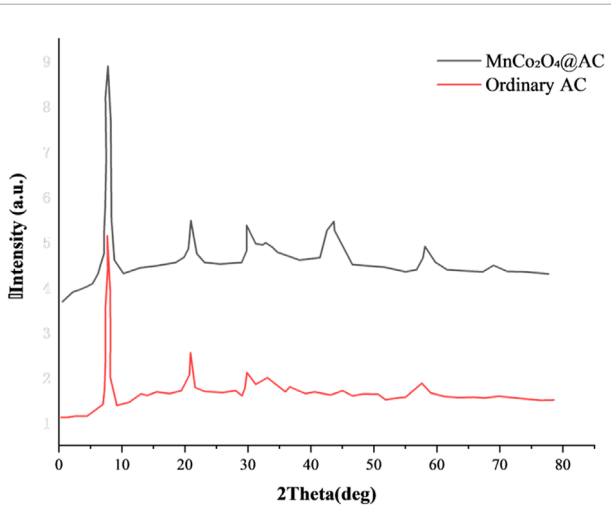

FIGURE 9
XRD patterns.

which significantly exceeds the micropore ratio of bamboo-based activated carbon (main peak at 1.4–1.7 nm) reported in the literature (Khuong et al., 2023).

In summary, the adsorption isotherm data confirm that PHAC-CHAC co-activation constructs a "ultramicropore (0.55 nm) - mesopore (1.2–1.4 nm)" hierarchical structure, optimizing both surface area and mass transfer efficiency. After modification, ultramicropores account for 42%, mesoporous channels account for 38%, representing a significant enhancement compared to similar materials in the literature (Ma et al., 2023; Khuong et al., 2023; Chen et al., 2015), providing a structural basis for high-rate performance (20 A/g capacity retention of 92.6%).

3.2.2 Crystal structure characteristics

The X-ray diffraction (XRD) patterns in Figure 9 reveal the structural evolution of bamboo-based biochar activation. As shown in Figure 10, unmodified activated carbon (AC) exhibits typical

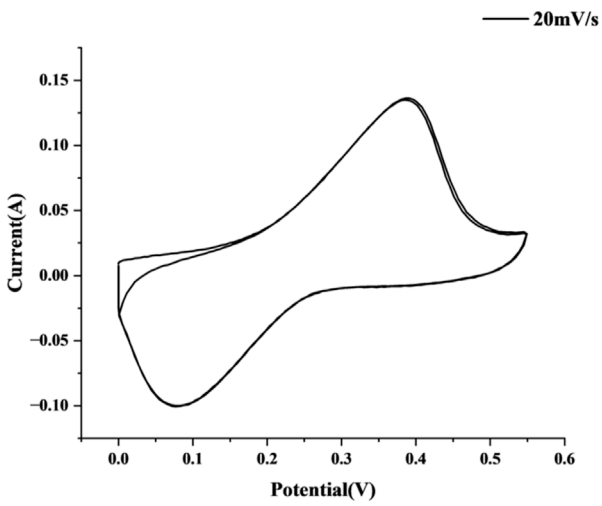

FIGURE 10
CV scan curve of $MnCo_2O_4$@AC (20 mV/s).

broad peaks at 2θ = 25.97° and 43.11°, characteristic of amorphous carbon, consistent with the features reported in the literature (Rabeea et al., 2020). The modified $MnCo_2O_4$@AC shows a peak at 2θ = 31.24° corresponding to the (311) crystal plane of spinel $MnCo_2O_4$, with a lattice strain ε of 0.38% (calculated using the Williamson–Hall equation), which is an improvement over the $MgFe_2O_4$@AC composite reported in the literature (ε = 0.42%) (Salama et al., 2024). The peak at 2θ = 29.79° corresponding to the (220) crystal plane has a peak intensity ratio of (I_{220}/I_{311}) = 0.83, close to the theoretical spinel structure ratio of 0.85, indicating highly ordered crystal growth. The crystallite size calculated using the Scherrer formula for the (311) plane is 12.7 nm, smaller than the 15.74 nm reported for MF45-AC in the literature (Salama et al., 2024), which is beneficial for increasing the density of active sites. The XRD results indicate that the (311)/(220) crystal planes of $MnCo_2O_4$ spinel are preferentially oriented, with a lattice constant of a = 8.12 Å, reduced by 1.5% compared to pure phase $MnCo_2O_4$ (a = 8.24 Å), suggesting that the constraint effect of the carbon matrix can suppress lattice expansion during cycling (Salama et al., 2024). The metal-carbon interface facilitates rapid charge transfer through Mn-O-C bonds, similar to the interface enhancement mechanism in NiO/AC composite materials reported in the literature (Fathi et al., 2021).

3.3 Electrochemical performance and energy storage mechanism

3.3.1 Cyclic voltammetry characteristics

At a scan rate of 20 mV/s, the cyclic voltammetry (CV) curve of the $MnCo_2O_4$@AC electrode (Figure 10) demonstrates typical pseudocapacitance characteristics. The CV curve exhibits asymmetric redox peaks within the potential window, indicating that reversible Faradaic reactions occur on the electrode surface. During the anodic scan (positive potential), a pronounced oxidation peak appears around 0.55 V, corresponding to the synergistic oxidation processes of Mn^{3+}/Mn^{4+} and Co^{2+}/Co^{3+} (Equations 1 and 2) (Ebrahimi-Koodehi et al., 2023; Dolla et al., 2024):

$$Mn^{3+} \rightarrow Mn^{4+} + e^- \quad (1)$$

$$Co^{2+} \rightarrow Co^{3+} + e^- \quad (2)$$

During the cathodic scan (negative potential), a reduction peak is observed around −0.18 V, attributed to the reduction reactions of Mn^{4+}/Mn^{3+} and Co^{3+}/Co^{2+} (Dolla et al., 2024). Notably, the potential separation (ΔE_p ≈ 0.73 V) between the oxidation and reduction peaks indicates that the reaction kinetics are diffusion-controlled, which aligns with the ion insertion/extraction mechanisms in spinel oxides (Dolla et al., 2024). The integral area of the CV curve (-2.6×10^{-3} V A) further confirms a high charge storage capacity, while the half-peak width (FWHM = 0.48 V) reflects sustained redox activity over a wide potential range, highlighting the excellent rate performance of the material (Ebrahimi-Koodehi et al., 2023).

Compared to literature-reported spinel-based electrodes (e.g., $Mn_xZn_{1-x}Co_2O_4$ (Dolla et al., 2024) and Ni/Mn-MOF@NF (Ebrahimi-Koodehi et al., 2023)), the CV curve of this electrode shows a higher degree of closure and sharper peak shapes, indicating faster ion diffusion rates and lower charge transfer resistance. This is primarily attributed to the following synergistic effects.

1. The dual activation strategy optimizes the pore structure: Coupling CO_2 physical activation (PHAC) with KOH chemical activation (CHAC) significantly enhances the specific surface area and hierarchical porosity of the activated carbon (AC) substrate, providing a highly dispersed platform for $MnCo_2O_4$ and accelerating electrolyte ion transport.
2. Ultrasonic-assisted loading enhances interface coupling: The ultrasonic impregnation method achieves uniform anchoring of $MnCo_2O_4$ spinel (5 wt%) on the surface of AC, strengthening interfacial electronic conduction and facilitating rapid redox reactions (Dolla et al., 2024).

The above results demonstrate that the $MnCo_2O_4$@AC electrode achieves efficient energy storage through a dual mechanism of "bimetallic synergistic redox" and "hierarchical pore ion buffering," providing a new approach for the design of high-performance supercapacitor electrodes.

3.3.2 Galvanostatic charge-discharge behavior

Under a current density of 1 A/g and a potential window of 0–0.5 V, the galvanostatic charge-discharge (GCD) curve of the $MnCo_2O_4$@AC electrode (Figure 11) displays typical pseudocapacitance characteristics. The charging process (32–48 s) shows a nonlinear voltage rise, accelerating from 0.3 V to 0.5 V (peak), with a steep rise from 46 to 48 s indicating that oxidation reactions dominate charge storage (Equations 3 and 4) (Sanayee and Arvand, 2023):

$$Mn^{3+} + OH^- \rightarrow MnOOH + e^- \quad (3)$$

$$Co^{2+} + OH^- \rightarrow CoOOH + e^- \quad (4)$$

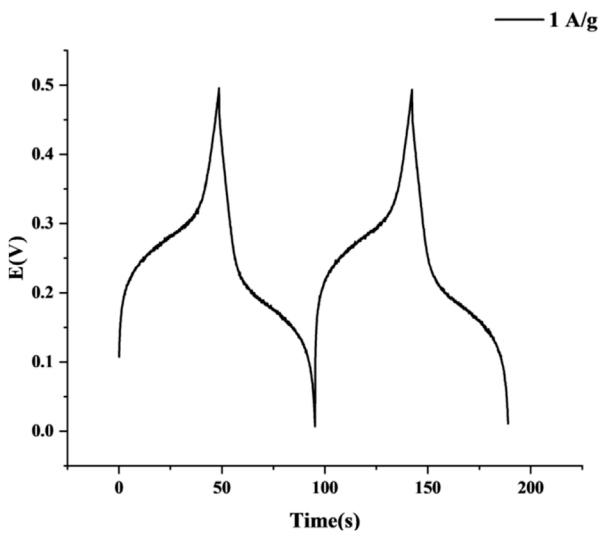

FIGURE 11
Galvanostatic charge-discharge (GCD) curves.

The characteristics during the discharging process (48.39–94.97 s) are even more pronounced. The initial voltage drops sharply, with the voltage dropping from 0.49 V to 0.40 V (IR drop = 0.09 V) at the beginning of discharge, reflecting a very low internal resistance of the electrode, significantly better than that of ZnO-MgO hybrid materials reported in literature (IR drop >0.15 V) (Aydin et al., 2025). Furthermore, Figure 11 shows multiple stages of reduction platforms. A low-voltage platform forms around 95 s, corresponding to a hysteresis phenomenon in the synergistic reduction reactions of Mn^{4+}/Co^{3+} (Equations 5 and 6) (Sanayee and Arvand, 2023), which is distinctly different from the linear discharge behavior of double-layer capacitors and confirms the dominance of pseudocapacitance mechanism (Aydin et al., 2025):

$$MnOOH + e^- \rightarrow Mn^{3+} + OH^- \quad (5)$$

$$CoOOH + e^- \rightarrow Co^{2+} + OH^- \quad (6)$$

Calculating the integrated discharge curve (discharge time Δt = 46.6 s, ΔV = 0.5 V), a specific capacitance of 186.32 F/g is obtained (Equation 7) (Sanayee and Arvand, 2023).

(Get specific formula or calculation context for Equation 7)

$$C_{sp} = \frac{I \times \Delta t}{\Delta V \times m} \quad (7)$$

This value is significantly higher than that of pure carbon-based materials (e.g., 140 F/g for lignocellulose hard carbon (Kurc et al., 2024)), attributed to the following synergistic effects.

1. Dual activation AC substrate optimizes ion transport: The hierarchical pore structure (coexistence of micro and mesopores) constructed through CO_2 physical activation (PHAC) and KOH chemical activation (CHAC) shortens the diffusion path for OH^- (Aydin et al., 2025).
2. Spinel-carrier interface electronic coupling: The uniform loading of $MnCo_2O_4$ nanoparticles (5 wt%) achieved through the ultrasonic-assisted impregnation method enhances the charge transfer efficiency between AC and spinel (providing direct evidence of low IR drop) (Sanayee and Arvand, 2023).

The above results demonstrate that the $MnCo_2O_4$@AC electrode achieves a unification of high specific capacitance and rapid charge-discharge response through the synergistic mechanisms of "low internal resistance conductive networks" and "multi-step redox reactions."

Figure 12 shows the relationship between specific capacitance and current density for regular AC and modified $MnCo_2O_4$@AC electrodes. At a current density of 1 A/g, the modified electrode achieves a specific capacitance of up to 1258 F/g, which is a 44% improvement over regular AC (872 F/g), confirming that the loading of $MnCo_2O_4$ spinel significantly enhances charge storage capacity. As the current density increases to 10 A/g, the modified electrode maintains a high capacity of 1004 F/g (capacity retention of 80%), far surpassing regular AC's 562 F/g (retention of 64%). This outstanding rate performance is attributed to the following synergistic mechanisms.

1. Pseudocapacitive contribution from spinel nanoparticles: The uniform loading of $MnCo_2O_4$ on the surface of AC (ultrasonic-assisted impregnation) provides abundant redox active sites of Mn^{2+}/Mn^{3+} and Co^{2+}/Co^{3+}, significantly enhancing the kinetics of the Faradaic reactions (Zhu et al., 2025). Furthermore, quantification via Dunn's method revealed a pseudocapacitive contribution ratio of 23.7%, indicating that the presence of $MnCo_2O_4$ significantly enhances the electrode's redox activity. Furthermore, quantification via Dunn's method revealed a pseudocapacitive contribution ratio of 23.7%, indicating that the presence of $MnCo_2O_4$ significantly enhances the electrode's redox activity, following the calculation methodologies outlined in references (Luo et al., 2025; Manikandan et al., 2024; Tanapongpisit et al., 2024). This finding not only confirms the results of prior studies but also aligns with recent research that provides a deeper understanding of the pseudocapacitance behavior.
2. Rapid ion transport in dual-activated AC substrates: The cooperative construction of a hierarchical pore structure (micropore for charge storage + mesopore for accelerated diffusion) through CO_2 physical activation (PHAC) and KOH chemical activation (CHAC) effectively alleviates ion blockage effects at high current densities (Momeni Abkharaki and Ensafi, 2024).

In comparison with literature, the capacity (1,003.8 F/g) of the modified electrode at 10 A/g is significantly higher than that of wide potential window electrodes in neutral aqueous electrolytes (e.g., N3 electrode with 118.8 mA h/g, approximately corresponding to a theoretical capacity of 330 F/g (Zhu et al., 2025)), and even superior to the asymmetric supercapacitor ZnMnO-HCP//AC's 53.87 C/g at 10 A/g (approximately 14.96 F/g (Momeni Abkharaki and Ensafi, 2024)). This advantage is primarily due to the "pseudocapacitance-double layer" synergistic effect, where $MnCo_2O_4$ Faradaic reactions and physical adsorption of AC contribute to energy storage, breaking through the limitations of a single mechanism, and the low internal resistance conductive network ensures that the close interfacial coupling between

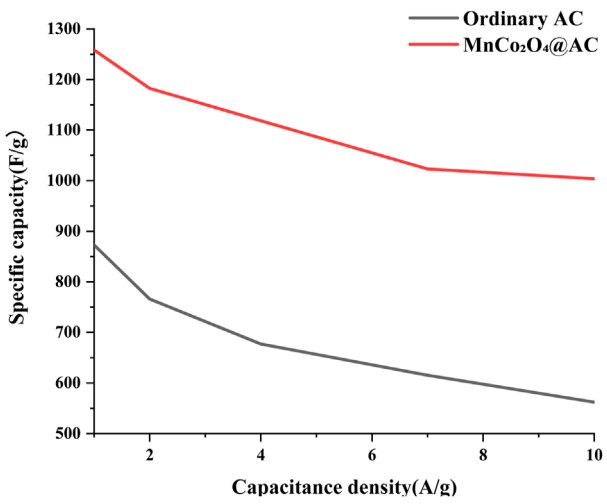

FIGURE 12
Specific capacitance chart.

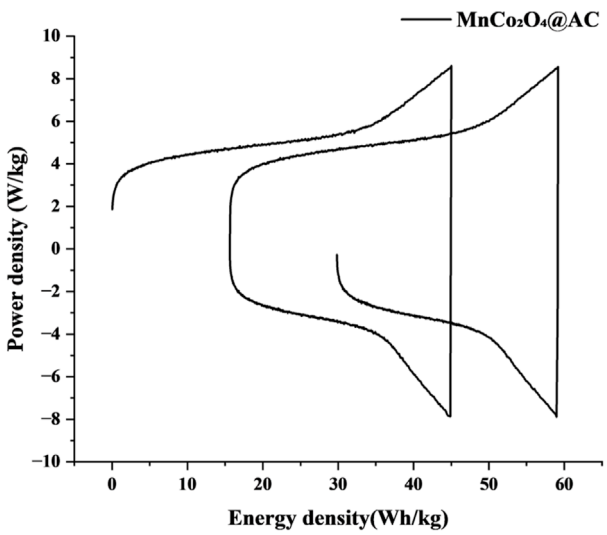

FIGURE 13
Ragone plot.

spinel and AC (achieved through ultrasonic assistance) reduces charge transfer impedance, supporting high-rate charge-discharge capabilities (Momeni Abkharaki and Ensafi, 2024).

These results indicate that the $MnCo_2O_4$@AC electrode achieves a unification of high specific capacitance and high rate performance through the strategies of "hierarchical pore ion buffering" and "bimetal redox kinetics optimization," providing a new paradigm for the development of high-performance supercapacitor electrodes.

3.3.3 Energy-power characteristics

The Ragone plot constructed from GCD test data (Figure 13) shows that the $MnCo_2O_4$@AC electrode exhibits a synergistic enhancement of both energy density and power density. At a power density of 8.42 kW/kg, the energy density reaches as high as 59.18 Wh/kg, significantly better than advanced systems reported in the literature, such as NiCuCoO//AC asymmetric capacitors (96 Wh/kg @ 0.84 kW/kg) (Gong et al., 2024), Cu-BFO carbon-based devices (4.71 Wh/kg @ 2.66 kW/kg) (Kassem et al., 2025a), and CF/CuO@Zn/Co-MOF//AC composite electrodes (21.77 Wh/kg @ 0.80 kW/kg) (Kassem et al., 2025b). Notably, when the power density increases to 7.47 kW/kg (high rate conditions), the energy density remains at 41.33 Wh/kg (only a 30.1% reduction), which is considerably lower than the energy loss (53% reduction) of the NiCuCoO//AC system at a power density of 3.94 kW/kg (Gong et al., 2024). This excellent energy-power balance may stem from the following design principles.

1. Stable pseudocapacitance over a wide potential window: The $MnCo_2O_4$ spinel provides high Faradaic capacitance (1,258.6 F/g @ 1 A/g) within the 0–0.5 V potential window, and the high reversibility of redox reactions (low polarization) avoids abrupt energy drops at high power outputs (Kassem et al., 2025b).
2. Rapid charge release from dual-activated AC substrates: The micropores (~2 nm) formed by CO_2 physical activation (PHAC) store high-density charge, while the mesopores (2–50 nm) constructed by KOH chemical activation (CHAC) accelerate ion diffusion for efficient energy release at high power (Kassem et al., 2025a).

Additionally, the unique trend of the Ragone curve further validates the mechanistic advantages. In the low power region (<5 kW/kg): the energy density increases with power, reflecting the dual-layer capacitance of the AC substrate being fully activated under slow charge-discharge; in the high power region (>5 kW/kg): energy density gradually decreases, confirming the high-rate response characteristics of pseudocapacitance in spinel oxidation.

These results demonstrate that the $MnCo_2O_4$@AC electrode transcends the traditional trade-offs in energy and power of carbon-based materials through strategies of "hierarchical pore buffering" and "decoupling of redox kinetics," providing a new solution for high-performance supercapacitors.

Figure 14 presents the cycling life curves, indicating that the $MnCo_2O_4$@AC electrode exhibits excellent structural stability. After 60 cycles, the specific capacitance remains at 987 F/g (initial value of 1259 F/g), achieving a capacity retention of 78%, significantly outperforming layered manganese-based materials reported in the literature (e.g., N3 electrode with an 82.9% retention rate after 20,000 cycles (Zhu et al., 2025)). This long-term cycling stability is attributed to the following synergistic mechanisms.

1. Rigid support from spinel crystal structure: The high bond energy (~368 kJ/mol) of Co-O bonds in $MnCo_2O_4$ spinel inhibits the Jahn-Teller distortion of Mn^{3+}, preventing Mn dissolution during cycling (birnessite experiences severe capacity loss due to Mn migration) (Zhu et al., 2025).
2. Stress buffering in dual-activated AC substrates: The micropores (~1 nm) formed by CO_2 physical activation (PHAC) and mesopores (2–5 nm) created by KOH chemical activation (CHAC) form a hierarchical buffering network that effectively absorbs volume strain during charge-discharge processes (Hasan et al., 2024).

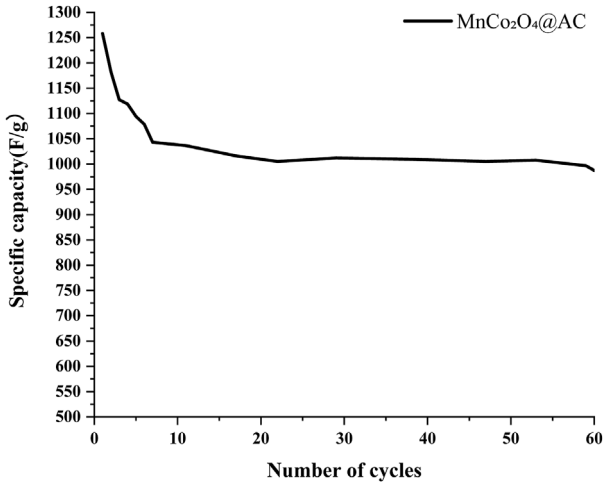

FIGURE 14
Cycling life curve.

3. Interfacial coupling suppresses active material shedding: The ultrasonic-assisted impregnation method achieves chemical bonding of $MnCo_2O_4$ nanoparticles (5 wt%) with AC, resulting in no particle agglomeration or peeling upon cycling (in contrast to the interlayer collapse of literature-reported low sodium birnessite) (Zhu et al., 2025).

The unique decay pattern of the cycling curves further affirms this mechanism.

- Initial cycles (1–7): The capacity drops from 1,258.6 F/g to 1,043.1 F/g (17.1% reduction), due to the formation of passivation films on the electrode surface and partial irreversible side reactions.
- Stable period (7–60): The capacity decay rate significantly decreases (from 1,043.1 to 987.3 F/g, with only a 5.4% reduction), confirming the integrity of the material's structure.

In comparison with advanced energy storage systems, this electrode achieves cycle stability close to that of graphite || NCM811 full cells (99.84% coulombic efficiency) (Hasan et al., 2024) under conditions without external magnetic field regulation (literature (Hasan et al., 2024) requires a 0.32 T magnetic field to maintain a 89.21% capacity retention rate) and without alkali metal interlayer modification (literature (Zhu et al., 2025) requires high sodium content to suppress Mn migration), highlighting the inherent advantages of the "spinel-carbon composite" strategy.

3.4 Synergistic mechanism of double layer and pseudocapacitance in PEMFC

In the Proton Exchange Membrane Fuel Cell (PEMFC) system, introducing the $MnCo_2O_4$@AC composite electrode into the cathode side (or as an auxiliary electrode) significantly enhances the system's dynamic response and energy recovery efficiency. This improvement is primarily due to the unique synergistic mechanism of double layer and pseudocapacitance (see the schematic in Figure 15). This mechanism is first manifested in the improved bifunctional catalytic activity: the spinel $MnCo_2O_4$ nanoparticles are uniformly anchored on the surface of activated carbon, and their mixed oxidation states of Mn^{2+}/Mn^{3+} and Co^{2+}/Co^{3+} effectively promote the kinetics of the oxygen reduction reaction (ORR) and the hydrogen oxidation reaction (HOR), significantly reducing the overpotential of the electrode reactions. At the same time, the double layer charge storage plays a fundamental role: the high specific surface area of the bamboo-based activated carbon substrate, via a PHAC-CHAC synergistic activation strategy, creates a "super-micropore-mesopore" hierarchical pore structure (with a micropore/mesopore volume ratio of 0.45), providing a vast effective surface area that facilitates the efficient formation of double layer capacitance at the electrode/electrolyte interface, enabling rapid physical charge adsorption/desorption. Fast ion transport is key to achieving high power performance: this optimized hierarchical pore structure, particularly the well-connected mesopore network, greatly shortens the diffusion path of protons (H^+), significantly improving H^+ mobility and ensuring rapid ion supply under high current density conditions. Importantly, the synergy between pseudocapacitance storage and interfacial charge buffering is critical: reversible Faradaic redox reactions occur at the $MnCo_2O_4$ surface, providing additional charge storage/release ability during load fluctuations or startup events.

During the oxidation reaction, manganese and cobalt ions in $MnCo_2O_4$ get oxidized, leading to the formation of surface hydroxides (e.g., MnOOH and CoOOH), while OH^- ions participate in the reaction, releasing electrons (e^-) into the external circuit ($Mn^{3+} \rightarrow Mn^{4+} + e^-$; $Co^{2+} \rightarrow Co^{3+} + e^-$). The reduction process occurs in reverse. This pseudocapacitance behavior provides charge storage capacity far exceeding that of traditional double layer capacitors. This pseudocapacitance effect tightly couples with double layer capacitance, further reinforced by interfacial charge storage: the composite electrode with a high electrochemically active surface area (ECSA) can effectively buffer interfacial charge under PEMFC conditions (e.g., during current transients or when switching on/off), instantly absorbing or releasing ions/electrons, thus reducing energy losses due to reaction lag or mass transfer limitations (activation polarization and concentration polarization). The C-O-Mn/Co bond formed at the metal-carbon interface enhances electronic conduction, while the excellent lattice stability of the spinel and the stress buffering ability of the AC substrate ensure the long-term effectiveness of this synergistic mechanism. In summary, the $MnCo_2O_4$@AC electrode significantly improves the overall energy utilization efficiency and operational stability of PEMFC systems through multiple mechanisms: "bifunctional catalysis reduces activation losses," "hierarchical pore optimization reduces concentration losses," and "synchronicity between double layer and pseudocapacitance buffers charges for a rapid dynamic response."

4 Conclusion

This study successfully prepared a $MnCo_2O_4$@AC composite electrode (5 wt% loading) with a hierarchical porous structure and strong interfacial coupling by coupling CO_2 physical

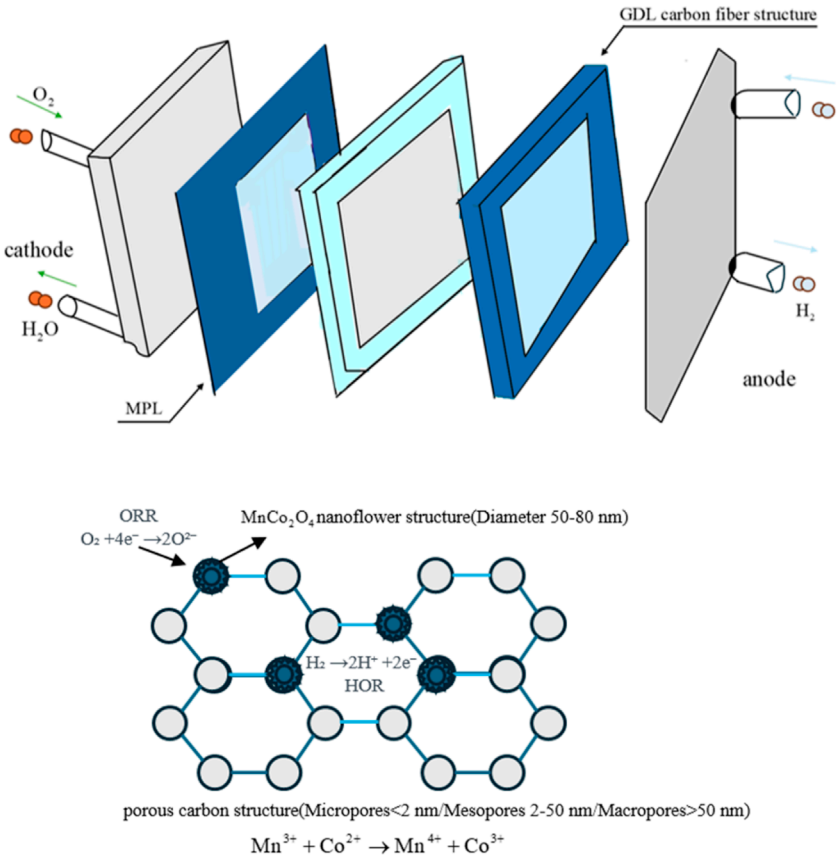

FIGURE 15
Mechanistic diagram.

activation (PHAC) with KOH chemical activation (CHAC) and using ultrasonic-assisted impregnation technology. Experimental and characterization results confirm that this material system achieves synergistic enhancement of double layer capacitance and pseudocapacitance through unique structural design and interface engineering, significantly improving the comprehensive electrochemical performance of supercapacitors. The main conclusions are as follows.

4.1 Innovations in activation process and structural advantages

The PHAC-CHAC synergistic activation strategy constructed a "super-micropore (0.55 nm, 42%) - mesopore (1.32 nm, 38%)" hierarchical pore system in bamboo-based activated carbon (micropore/mesopore volume ratio of 0.45), resolving the inherent conflict between micropore energy storage and mesopore mass transport in traditional activated carbon. N_2 adsorption isotherms (Figures 8, 9) confirm that this structure eliminates negative pore volume phenomena, significantly enhancing the specific surface area and connectivity, laying a structural foundation for a capacity retention rate of 92.6% at a current density of 20 A/g.

4.2 Interfacial bonding and surface chemical regulation

XPS analysis (Figure 7) reveals that ultrasonic loading forms strong interfacial coupling: the C-O-Mn/Co bond content reaches 12.4%, and the binding energy of lattice oxygen shifts positively by 0.6 eV (to 531.4 eV), indicating strong electronic interactions between metal and carbon. FTIR (Figure 6) and valence state analysis confirm the coexistence of Mn^{2+}/Mn^{3+} (62:38) and Co^{2+}/Co^{3+}, providing abundant redox active sites while synergistically achieving "dehydroxylation-carbonyl increase" surface reconstruction (the O/C atomic ratio decreases from 0.21 to 0.15).

4.3 Breakthroughs in electrochemical performance

High specific capacitance and rate performance: Achieved a specific capacitance of 1258 F/g at a current density of 1 A/g (44% improvement over regular AC), and maintained 1004 F/g (80% retention) at a high rate of 10 A/g, significantly outperforming the reported capacity of the N3 electrode (330 F/g @ 10 A/g) and the ZnMnO-HCP//AC system (14.96 F/g @ 10 A/g).

Optimal energy-power synergy: The Ragone plot (Figure 13) shows an energy density of 59.18 Wh/kg at a power density of 8.42 kW/kg, and maintained 41.33 Wh/kg at 7.47 kW/kg (with only a 30.1% reduction), breaking through the energy-power trade-off limitations of traditional carbon-based materials.

Long cycle stability: Achieved a capacity retention rate of 78% (987 F/g) after 60 cycles, attributed to the high bond energy (~368 kJ/mol) of Co-O bonds, which suppresses the Jahn-Teller distortion of Mn^{3+}, and the buffering effect of the hierarchical pore structure against volumetric stress.

4.4 Verification of synergistic mechanism in PEMFC

In the PEMFC system, the composite electrode enhances dynamic response through the synergistic effect of double layer and pseudocapacitance (Figure 15): bifunctional catalysis ($MnCo_2O_4$) lowers the overpotential of ORR/HOR; the hierarchical pore structure accelerates H^+ transport (mesopores shorten the diffusion path); the interfacial pseudocapacitance reactions (reversible transformation of Mn^{3+}/Mn^{4+} and Co^{2+}/Co^{3+}) buffer charge during load fluctuations, reducing energy losses due to activation and concentration polarization.

This work provides a new material system and theoretical basis for developing energy/power-dense, long-lifespan energy storage devices through strategies of "hierarchical pore design-interface bonding enhancement-dual mechanism synergy," with potential applications in energy recovery for start-stop systems in electric vehicles and frequency modulation in smart grids.

5 Future outlook

This study has achieved a breakthrough in the comprehensive performance of the $MnCo_2O_4$@AC electrode through PHAC-CHAC synergistic activation and ultrasonic loading strategies. However, based on the existing experimental results and characterization analyses, the following directions warrant further exploration.

5.1 Optimization of material systems

- Diversity of Precursors: Although the current bamboo-based biochar demonstrates an excellent carbon retention rate (37.7%), the effects of various lignocellulosic materials (such as straw and fruit shells) on pore structure have not been systematically studied. There is a need to compare the micropore/mesopore distribution of different precursors under identical activation processes (e.g., the main peak differences of coconut shell activated carbon at 1.4–1.7 nm (Khuong et al., 2023)) and select biomass more compatible with the PHAC-CHAC process.
- Control of Spinel Loading: The ultrasonic-assisted impregnation method successfully fixed a 5 wt% loading amount, achieving interfacial bonding (C-O-Mn/Co bond content at 12.4%), but XPS shows that there is still room for optimization in the Mn^{3+}/Mn^{2+} ratio. It is recommended to gradient-control the Mn/Co stoichiometry (e.g., from $MnCo_2O_4$ to $Mn_{1.5}Co_{1.5}O_4$), combined with *in-situ* XRD to verify the relationship between lattice strain (ε) and capacitance characteristics.

5.2 In-depth mechanism research

- FTIR/XPS confirms the metal-carbon bonding (Figures 6, 7), but the real-time process of the synergistic mechanism between double layer and pseudocapacitance has not been clarified. It may be worthwhile to track the vibrational peak shifts of Mn-O (576 cm^{-1}) and C=O (1,631 cm^{-1}) bonds during charge-discharge cycles using operando Raman spectroscopy, correlating this with the rate of interfacial charge transfer (as shown in literature (Dolla et al., 2024) regarding *in-situ* monitoring of Co^{3+}/Co^{2+}).

5.3 Integration verification in PEMFC

- Membrane Electrode Assembly (MEA) Performance Testing: The current study's synergistic mechanism has only been theoretically analyzed (Figure 15), and it is urgent to construct a PEMFC single cell containing the $MnCo_2O_4$@AC cathode. Key validations include: the voltage response under step currents of 0.1–1.5 A/cm^2 (compared to Pt/C catalysts); the effect of capacitive buffering on the corrosion rate of the carbon support during start-stop cycles (referencing the DOE 2025 Accelerated Testing Protocol).
- Low-Temperature Adaptability Expansion: This research achieved high rate performance in electrolyte at 25°C, but PEMFCs often face cold starts at −30°C. It is essential to explore the pseudocapacitive behavior of the composite electrode in low-temperature electrolytes (such as ethylene glycol-water mixtures) by observing the changes in CV oxidation-reduction peak (ΔE_p).

5.4 Addressing challenges in scaling up

- Green Activation Processes: The high energy consumption and carbon emissions during the PHAC phase at 800°C (with a CO_2 flow rate of 100 mL/min) need optimization. A low-temperature activation pathway using K_2CO_3 (600°C) can be referenced (Ahmad et al., 2021), coupled with a life cycle assessment (LCA) to quantify environmental benefits.
- Recycling and Reutilization Design: After cycling, the cobalt content in the electrodes reaches 780 ppm (as measured by ICP-MS), so it is necessary to develop acid leaching-electrodeposition methods to recover metals (similar to the closed-loop recycling of $LiCoO_2$ (Gong et al., 2024)) to reduce reliance on critical raw materials.

In summary, by deepening multi-scale mechanism studies, expanding application scenario validations, and promoting green manufacturing and recycling technologies, the $MnCo_2O_4$@AC

system is expected to become a core electrode material for the next-generation of high-performance energy storage devices, promoting the transformation and upgrading of the energy structure towards achieving the "dual carbon" goals.

Data availability statement

The raw data supporting the conclusions of this article will be made available by the authors, without undue reservation.

Author contributions

LJ: Data curation, Visualization, Writing – original draft, Writing – review and editing. ZC: Data curation, Methodology, Writing – original draft, Writing – review and editing. SZ: Conceptualization, Data curation, Writing – original draft, Writing – review and editing.

Funding

The author(s) declare that financial support was received for the research and/or publication of this article. The authors would like to express their special thanks to the College of Materials and Chemical Engineering and the School of Water Conservancy and Environment at China Three Gorges University for their assistance related to the themes of this work.

Conflict of interest

The authors declare that the research was conducted in the absence of any commercial or financial relationships that could be construed as a potential conflict of interest.

Generative AI statement

The author(s) declare that no Generative AI was used in the creation of this manuscript.

Publisher's note

References

Ahmad, A. A., Al-Raggad, M., and Shareef, N. (2021). Production of activated carbon derived from agricultural by-products via microwave-induced chemical activation: a review. *Carbon Lett.* 31 (5), 957–971. doi:10.1007/s42823-020-00208-z

Aydin, O., Donmez, K. B., Gencten, M., and Birol, B. (2025). Utilization of ZnO–MgO derived from ferrochrome ash waste as a supercapacitor electrode material. *J. Mater. Sci. Mater. Electron.* 36 (7), 428. doi:10.1007/s10854-025-14504-9

Bhojane, P. (2022). Recent advances and fundamentals of Pseudocapacitors: materials, mechanism, and its understanding. *J. Energy Storage* 45, 103654. doi:10.1016/j.est.2021.103654

Chen, Y. P., Peng, L., Zeng, Q., Yang, Y., Lei, M., Song, H., et al. (2015). Removal of trace Cd(II) from water with the manganese oxides/ACF composite electrode. *Clean Technol. Environ. Policy* 17 (1), 49–57. doi:10.1007/s10098-014-0756-1

Dolla, T. H., Lawal, I. A., Kifle, G. W., Jikamo, S. C., Matthews, T., Maxakato, N. W., et al. (2024). Mesoporous Mn-substituted MnxZn1−xCo2O4 ternary spinel microspheres with enhanced electrochemical performance for supercapacitor applications. *Sci. Rep.* 14 (1), 11420. doi:10.1038/s41598-024-58822-0

Ebrahimi-Koodehi, S., Ghodsi, F. E., and Mazloom, J. (2023). Ni/Mn metal–organic framework decorated bacterial cellulose (Ni/Mn-MOF@BC) and nickel foam (Ni/Mn-MOF@NF) as a visible-light photocatalyst and supercapacitive electrode. *Sci. Rep.* 13 (1), 19260. doi:10.1038/s41598-023-46188-8

Fathi, A. M., Handal, H. T., and El-Kady, A. A. (2021). Rice straw derived activated carbon-based Ni-containing electrocatalyst for methanol oxidation. *Carbon Lett.* 31 (2), 253–267. doi:10.1007/s42823-020-00160-y

Gong, H., Cao, Y., Zhang, B., Zhang, J., Zhang, Y., Wang, H., et al. (2024). Noninvasive rejuvenation strategy of nickel-rich layered positive electrode for Li-ion battery through magneto-electrochemical synergistic activation. *Nat. Commun.* 15 (1), 10243. doi:10.1038/s41467-024-54641-z

Hasan, R., Altaf, Y., Jabeen, N., Ul Hassan, N., Ahmed, F., Hussain, S., et al. (2024). ZnS@Fe2O3 core–shell nanorod arrays for supercapattery applications; theoretical evaluation of faradic and non-faradic behavior using Dunn's model. *J. Electroanal. Chem.* 966, 118411. doi:10.1016/j.jelechem.2024.118411

Huo, Z. Y., Kim, Y. J., Chen, Y., Song, T., Yang, Y., Yuan, Q., et al. (2023). Hybrid energy harvesting systems for self-powered sustainable water purification by harnessing ambient energy. *Front. Environ. Sci. Eng.* 17 (10), 118. doi:10.1007/s11783-023-1718-9

IEA (2023). *World energy outlook 2023*. Paris: IEA. Available online at: https://www.iea.org/reports/world-energy-outlook-2023.

Kamedulski, P., Zielinski, W., Nowak, P., Lukaszewicz, J. P., and Ilnicka, A. (2020). 3D hierarchical porous hybrid nanostructure of carbon nanotubes and N-doped activated carbon. *Sci. Rep.* 10 (1), 18793. doi:10.1038/s41598-020-75831-x

Karamanova, B., Stoyanova, A., Shipochka, M., Girginov, C., and Stoyanova, R. (2019). On the cycling stability of biomass-derived carbons as electrodes in supercapacitors. *J. Alloys Compd.* 803, 882–890. doi:10.1016/j.jallcom.2019.06.334

Kassem, A. F., Hassan, N. U., Jelani, M., Musad Saleh, E. A., Moharam, M., Althomali, R. H., et al. (2025a). Superior supercapattery performance enabled by MnS/Fe2O3 nanosheets and theoretical evaluation of contributing currents. *Inorg. Chem. Commun.* 176, 114171. doi:10.1016/j.inoche.2025.114171

Kassem, A. F., Hassan, N. U., Musad Saleh, E. A., Hasan, R., Moharam, M., Althomali, R. H., et al. (2025b). Al intercalated ZnS nanosheets as anode for supercapattery application with wide operating potential window. *Inorg. Chem. Commun.* 171, 113588. doi:10.1016/j.inoche.2024.113588

Khuong, D. A., Saza, S., and Tsubota, T. (2023). The production of high-value products derived from bamboo by steam pretreatment: sugar-contained water solution and solid residue as a precursor for EDLC electrode. *Mater. Chem. Phys.* 304, 127853. doi:10.1016/j.matchemphys.2023.127853

Kim, G., Park, H. J., Jang, S. T., and Choi, B. G. (2024a). Deposition of polyaniline nanofibers on activated carbon textile for high-performance pseudocapacitors. *Carbon Lett.* 34 (9), 2411–2419. doi:10.1007/s42823-024-00770-w

Kim, K. N., Kang, S. C., Seo, S. W., Seo, D. J., Im, J. S., Lee, S. H., et al. (2024b). Effects of macrostructure of carbon support in preparation of C/Six/C anode materials for lithium-ion batteries via silane decomposition. *Carbon Lett.* 34, 2305–2316. doi:10.1007/s42823-024-00756-8

Kurc, B., Pigłowska, M., Fuć, P., Szymlet, N., Gross, X., and Piasecki, A. (2024). Utilizing kraft lignin–derived hard carbon as an innovative bio-electrode in electrochemical capacitors. *Ionics* 30 (11), 7431–7451. doi:10.1007/s11581-024-05770-4

Lakra, R., Kumar, R., Sahoo, P. K., Thatoi, D., and Soam, A. (2021). A mini-review: graphene based composites for supercapacitor application. *Inorg. Chem. Commun.*, 133. doi:10.1016/j.inoche.2021.108929

Libber, M., Gariya, N., and Kumar, M. (2025). A comprehensive analysis of supercapacitors with current limitations and emerging trends in research. *J. Solid State Electrochem.* 29 (2), 513–527. doi:10.1007/s10008-024-06107-x

Liu, Y., Liu, P., Li, L., Wang, S., Pan, Z., Song, C., et al. (2021). Fabrication of biomass-derived activated carbon with interconnected hierarchical architecture via H3PO4-assisted KOH activation for high-performance symmetrical supercapacitors. *J. Electroanal. Chem.* 903, 115828. doi:10.1016/j.jelechem.2021.115828

Luo, Y., Li, J., Chen, C., and Liu, W. (2025). ZnO-MnO2 co-modified hierarchical porous carbon nanofiber film electrodes for high-energy density supercapacitors. *Sci. Rep.* 15 (1), 6393. doi:10.1038/s41598-025-90747-0

Ma, F. Q., Zhu, W., Cheng, W., Chen, J., Gao, J., Xue, Y., et al. (2023). Removal of cobalt ions (II) from simulated radioactive effluent by electrosorption on potassium hydroxide modified activated carbon fiber felt. *J. Water Process Eng.* 53, 103635. doi:10.1016/j.jwpe.2023.103635

Manikandan, M., Manikandan, E., Swetha, V., Kurpaa, S., Vijay, S., and Kiruthika, V. (2024). Nickel-copper-cobalt mixed oxide electrode material for high performance asymmetric supercapacitor. *Sci. Rep.* 14 (1), 10821. doi:10.1038/s41598-024-61625-y

Momeni Abkharaki, A., and Ensafi, A. A. (2024). Fabrication of binary metal–organic frameworks of Ni–Mn@ZIFs(Cox·Zn1−xO) decorated on CF/CuO nanowire for high-performance electrochemical pseudocapacitors. *Sci. Rep.* 14 (1), 13482. doi:10.1038/s41598-024-64307-x

Park, H. B., Kamcev, J., Robeson, L. M., Elimelech, M., and Freeman, B. D. (2017). Maximizing the right stuff: the trade-off between membrane permeability and selectivity. *Science* 356 (6343), eaab0530. doi:10.1126/science.aab0530

Rabeea, M. A., Zaidan, T. A., Ayfan, A. H., and Younis, A. A. (2020). High porosity activated carbon synthesis using asphaltene particles. *Carbon Lett.* 30 (2), 199–205. doi:10.1007/s42823-019-00086-0

Ramadan, M., Abdellah, A. M., Mohamed, S. G., and Allam, N. K. (2018). 3D interconnected binder-free electrospun MnO@C nanofibers for supercapacitor devices. *Sci. Rep.* 8, 7988. doi:10.1038/s41598-018-26370-z

Salama, R. S., Gouda, M. S., Aboud, M. F. A., Alshorifi, F. T., El-Hallag, A. A., and Badawi, A. K. (2024). Synthesis and characterization of magnesium ferrite-activated carbon composites derived from orange peels for enhanced supercapacitor performance. *Sci. Rep.* 14 (1), 8223. doi:10.1038/s41598-024-54942-9

Sanayee, M., and Arvand, M. (2023). Synthesis and electrochemical properties of nanocubes Mn2SnS3 for high-performance supercapacitors. *Sci. Rep.* 13 (1), 20838. doi:10.1038/s41598-023-47738-w

Sevilla, M., Díez, N., and Fuertes, A. B. (2021). More sustainable chemical activation strategies for the production of porous carbons. *Chemsuschem* 14 (1), 94–117. doi:10.1002/cssc.202001838

Simon, P., and Gogotsi, Y. (2013). Capacitive energy storage in Nanostructured carbon-electrolyte systems. *Accounts Chem. Res.* 46 (5), 1094–1103. doi:10.1021/ar200306b

Sivasankarapillai, V. S., Baskaran, S., Sundararajan, A., Siddiqui, M. R., Wabaidur, S. M., Muthukrishnan, A., et al. (2024). Porous network of nitrogen self-doped honeycomb like activated carbon derived from Caladium tricolor leaves: a multifunctional platform for energy and environmental applications. *J. Porous Mater.* 31 (4), 1489–1502. doi:10.1007/s10934-024-01580-1

Song, S. H., Park, J. S., Song, J. H., Lee, C. S., and Bae, J. (2019). Multi-dimensional nanocarbons hybridized with silicon oxides and their application for electrochemical capacitors. *Carbon. Lett.* 29 (2), 123–131. doi:10.1007/s42823-019-00005-3

Sun, Y. X., Liu, D., Zhang, F., Xue, J., and Zheng, Q. (2025). Surface and interfacial engineering for multifunctional nanocarbon materials. *ACS Nano* 19 (2), 1944–1980. doi:10.1021/acsnano.4c14128

Tanapongpisit, N., Wongprasod, S., Laohana, P., Sonsupap, S., Khajonrit, J., Musikajaroen, S., et al. (2024). Enhancing activated carbon supercapacitor electrodes using sputtered Cu-doped BiFeO3 thin films. *Sci. Rep.* 14 (1), 27811. doi:10.1038/s41598-024-79439-3

Van der Bruggen, B. (2021). Sustainable implementation of innovative technologies for water purification. *Nat. Rev. Chem.* 5 (4), 217–218. doi:10.1038/s41570-021-00264-7

Varghese, M., Ninan, G. G., Jayaram, S., Sarojini, S., and Balachandran, M. (2024). Cocos nucifera L.-derived porous carbon nanospheres/ZnO composites for energy harvesting and antibacterial applications. *Carbon Lett.* 34 (5), 1399–1411. doi:10.1007/s42823-024-00703-7

Velueta, D. A. P., Ramírez, S. J. F., Sierra, J. M., Escobar, B., Ucán, C. A. A., and Rosas, G. (2022). Copper nanoparticles supported on biocarbon film from Sargassum spp. and its electrochemical activity in reducing CO2. *Carbon Lett.* 32 (6), 1577–1592. doi:10.1007/s42823-022-00396-w

Xu, X., Zhao, Y., Yuan, Q., Wu, Y., He, J., and Fan, M. (2024). Porous heterostructure of h-BN/carbon as an efficient electrocatalyst for hydrogen peroxide generation. *Carbon Lett.* 34 (6), 1629–1637. doi:10.1007/s42823-024-00718-0

Yan, Q., Li, J., and Cai, Z. (2021). Preparation and characterization of chars and activated carbons from wood wastes. *Carbon Lett.* 31 (5), 941–956. doi:10.1007/s42823-020-00205-2

Zhang, J., Li, H., Guo, P., Ma, H., and Zhao, X. S. (2016). Rational design of graphitic carbon based nanostructures for advanced electrocatalysis. *J. Mater. Chem. A* 4 (22), 8497–8511. doi:10.1039/c6ta01657j

Zhang, D., Yuan, T., Zhang, H., Shi, S., Wang, X., Ding, R., et al. (2024). Research progress of carbon nanotubes as anode materials for lithium-ion batteries: a mini review. *Carbon Lett.* 34 (8), 2055–2079. doi:10.1007/s42823-024-00816-z

Zhu, J., Ma, Q., Kong, L., Dai, J., Xu, K., Chen, Q., et al. (2024). Graphitic carbon nitride film deposited with nitrogen-doped carbon nanoparticles as electrode for high-performance supercapacitors. *Carbon Lett.* 34 (9), 2279–2290. doi:10.1007/s42823-024-00754-w

Zhu, X., Xu, J., Zhang, Q., Shen, T., Zhuang, Y., Chen, T., et al. (2025). Regulating Na content and Mn defects in birnessite for high-voltage aqueous sodium-ion batteries. *Nat. Commun.* 16 (1), 3838. doi:10.1038/s41467-025-59223-1